Received: 26 June 2022 | Revised: 20 March 2023 | Accepted: 21 March 2023

DOI: 10.1002/nag.3527

RESEARCH ARTICLE

WILEY

A hydro-mechanically-coupled XFEM model for the injection-induced evolution of multiple fractures

Yuxiao Wang[1] | **Akbar A. Javadi**[1] | **Corrado Fidelibus**[1,2]

[1]Department of Engineering, University of Exeter, Exeter, UK

[2]Dipartimento di Ingegneria dell'Innovazione, Università del Salento, Lecce, Italy

Correspondence
Akbar A. Javadi, University of Exeter, Exeter EX4 4QF, UK.
Email: A.A.Javadi@exeter.ac.uk

Abstract

In this paper, a two-dimensional eXtended Finite Element Method (XFEM) solution is presented for the hydro-mechanically coupled hydro-frac-induced propagation of multiple fractures in rocks. Fractures are considered one-dimensional objects, and the rock matrix is regarded as a two-dimensional medium. Rules for improving the accuracy of the solution are included to deal with the transfer of variables between fractures and matrix in the coupling process. The main variables include fluid pressure and fracture aperture. The following assumptions are made: (1) the fluid pressure inside a fracture is applied as a net pressure; (2) fluid leak-off is ignored; (3) the fluid front is regarded as a fracture front provided that the area of fluid lag has a small effect on fracture propagation compared to the area at which the fluid pressure is applied. The fluid flow is governed by the lubrication equation, while the XFEM is used to describe the behaviour of the elastic medium. The simulation results are compared with analytical solutions for a single hydraulic fracture model to verify and validate the proposed algorithm. A simulation with multiple hydraulic fractures is also performed to investigate the interference effect of multiple fractures and fracture propagation. The shadow effect caused by multiple fractures is analysed to manifest the stress variation along the propagation path.

KEYWORDS

eXtended Finite Element Method (XFEM), fracture propagation, hydro-mechanically coupled process, multiple fractures

1 | INTRODUCTION

Hydraulic fracturing (hydro-frac) has been widely developed in the past decades and has become an important tool -to improve the oil/gas production in unconventional reservoirs.[1] At present, many companies apply this method to complex formations and deep wells.[2] In a hydro-frac process, a highly pressurised fluid (frac-fluid) is pumped into a wellbore to activate the opening of artificial fractures in the target formation in order to enhance the conductivity and ease the extraction of oil/gas. A reliable and robust estimation of the induced propagation of these artificial fractures can help adjust and optimise operation schemes in the field.

The research on fluid-driven fracturing has drawn much attention from academics worldwide. In the last decades, many findings have been reported concerning the improvement of hydro-frac processes, with focus on the models for the prediction of fluid-driven fracture initiation and propagation. The early proposed models include the Khristianovic–Geertsma–de Klerk (KGD) model[3,4] and the Perkins–Kern–Nordgren (PKN) model,[5,6] which still play an important role in guiding field operations. Contributions refer to the results of laboratory tests set up to understand the physics underpinning the hydro-frac processes. Hubbert and Willis[7] stated that fractures approximately propagate in the direction perpendicular to the maximum principal stress. Clifton and Abou-Sayed,[8] and Abou-Sayed[9] developed the first three-dimensional fracture propagation model. Abass et al.[10] studied non-planar fracture geometries in laboratory experiments and defined a correlation between the breakdown pressure and the wellbore orientation. Ma et al.[11] used a triaxial apparatus to simulate the hydro-frac in a glutenite reservoir and found that the propagation is enclosed within microzones of high-strength gravel particles, generating narrow and terminated fractures. He et al.[12] used x-ray spectrometry in sandstone specimens to demonstrate the dominant role in the width evolution of hydraulic fractures. Chitrala et al.[13] studied the hydro-frac-induced propagation under different stresses in dense sands by using acoustic emissions and showed that the propagation is not continuous.

A wide range of numerical methods has been developed to simulate fracture initiation and propagation, including mainly the Finite Element Method (FEM), the Discrete Element Method (DEM) and the eXtended Finite Element Method (XFEM). Few contributions refer to the Finite Difference Method (FDM)[14] and the Boundary Element Method (BEM),[15]

In the context of FEM, Ng and Small[16] adopted FEM for the prediction of HF occurring in cores of rock dams. Khoei et al.[17] developed an enriched FEM technique to simulate the interaction between hydraulic and natural fractures in impervious media, also analysing the effect of the fluid viscosity. In addition, cohesive crack models gained popularity for the simulation of hydro-frac propagation, also dealing with artificial fractures intersecting pre-existing ones.[18,19]

Among the applications of DEM, Yoon et al.[20] used a 2D Particle Flow Code (PFC) to simulate arrest, crossing and dilation of hydraulic and natural fractures in low-permeability hard rocks. Lavrov et al.[21] developed a hybrid FEM/DEM simulator to simulate HF in naturally fractured reservoirs under isotropic and anisotropic in situ stress; they found that for an isotropic in-situ stress field, the pattern of generated fractures is strongly mesh-dependent.

Other contributions refer to somewhat hybrid methods, being combinations of the above-mentioned methods; the following are worth mentioning: Zeng et al.[22] developed an EDFM–XFEM approach and defined a hydro-thermally coupled elasto-plastic model for HF in saturated porous media; they showed that plastic deformations can increase the fracture propagation pressure and decrease the propagation velocity; Wong et al.[23] proposed a non-planar 3D model to study the interaction of multiple hydraulic fractures generated from a horizontal well; the influence of the stress shadow on the propagation of multiple fractures was also analysed; finally, Cordero et al.[24] proposed an innovative mesh fragmentation technique to simulate HF along arbitrary paths and intersections with frictional natural fractures; they studied the dependence of the propagation process on the fracture friction angle.

Compared with the other methods, XFEM is rather new and represents a great prospect for such simulations, mainly because remeshing and mesh refinement, unlike the standard FEM model, are avoided by adding enrichment functions to the nodes of the fracture elements to better reproduce the discontinuity as the fracture propagates, so a large amount of computational time and cost can be saved.

Several applications of XFEM to hydro-frac processes are available. Adachi et al.[25] defined the physico-mathematical statements of hydro-frac and discussed issues concerning the numerical simulations, including tracking of the fracture footprint, and coupling of the equations. Lecampion[26] used XFEM to study two hydro-frac propagation regimes, the toughness-dominated and the viscosity-dominated, and highlighted the importance of correcting the loss of partition of unity in the transition zone between the enriched part and the rest of the mesh. Shi et al.[27] proposed a technique for the simultaneous solution of the equilibrium and fluid continuity equations in the framework of a fully hydro-mechanically (HM) coupled model with natural fractures; by resorting to this technique, the authors claim that a significant reduction of the simulation time can be achieved with acceptable convergence rates. Gordeliy and Peirce[28] developed two XFEM schemes based on the implicit level set algorithm for locating the free boundary when the fluid and fracture front coalesce. XFEM was also used by Sheng et al.[29] to study multi-stage hydro-frac in anisotropic shales, deducing that propagation trajectories are more influenced by the local stress field at the tips of the fractures than the in situ stress field, and by Jafari et al.[30] to assess the effect of fluid loss on the efficiency of hydro-frac saturated porous media by using an HM coupled model. Zheng et al.[31] established a hydro-frac propagation model using XFEM based on a damage–stress–seepage coupling to analyse the influence of the approach angle of an existing natural fracture and of the horizontal stress difference on the propagation; it was shown that the degree of opening of the natural fractures increases with the decrease of the approaching angle and of the horizontal differential stress. Cruz et al.[32] proposed a formulation comprising fracture intersection and crossing, and fracture frictional behaviour to study the influence of natural fractures on hydro-frac

TABLE 1 Glossary of terms.

a	Fracture initial length in the examples
$\mathbf{a}, \mathbf{b}$	Additional degrees of freedom (dofs) for the enriched nodes
$\mathbf{B}$	Strain differential operator matrix
d	distance between an element node and a fracture node
$\mathbf{D}$	Matrix of the elasticity coefficients
e	Fracture aperture (also the maximum value)
E	Young's elastic modulus
h, w	Dimensions of the domains in the examples
H	Jump function
$\mathbf{K}$	Global stiffness matrix
K_1, K_2	SIF values for Mode-I and Mode-II, resp.
$\mathbf{n}, \mathbf{n}_\mathrm{f}$	Unit vectors normal to Γ e Γ_f, resp.
N_f	Number of nodes in a fracture
N^cut	Set of enriched nodes of the elements crossed by a fracture
N_i	Standard shape functions
N^s	Number of standard nodes
N^tip1	Set of enriched nodes of the first crack tip
N^tip2	Set of enriched nodes of the second crack tip
p	Fluid pressure
$\mathbf{P}$	right-hand side vector of the final equation system
q_ξ	Fluid discharge per unit fracture width along ξ
Q_0	Fluid volumetric source at the injection point
r, θ	Polar coordinates with origin at the crack tip
s	Spacing among fractures
SIF	Stress intensity factor
$\mathbf{t}$	Boundary tractions
t	Time
$\mathbf{u}$	Displacements
$\bar{\mathbf{u}}$	Prescribed displacement on $\Gamma_\mathbf{u}$
$\Gamma, \Gamma_\mathbf{t}, \Gamma_\mathbf{u}$	Boundary of Ω, portions of Γ with prescribed tractions and displacements, resp.
Γ_f	Boundary of a fracture
δ	Dirac delta function
ϵ	Strain tensor
μ	Fluid dynamic viscosity
ν	Poisson's ratio
ν_f	Number of fractures
ξ	Local coordinate of a fracture
ξ_0	Fracture local coordinate of the injection point
$\boldsymbol{\sigma}$	Stress tensor
$\phi(x, y)$	Signed distance function
$\psi^{(1)}, \psi^{(2)}$	Tip branch functions at the first and at the second crack tip
Ω	Analysis domain

propagation; they found that the hydraulic response is very sensitive to parameters such as the in situ stress and the angle between the fractures.

The above-mentioned works have not fully considered the coupling effect and element interaction between two types of media, including the stress transfer between the fluid and matrix and the change of aperture (and transmissivity) with the decreasing fluid pressure (leading to an indirect HM-coupled process). Also, few proposed HM-coupled models to deal with multiple fractures. In this paper, with reference to multiple artificial fractures, a novel XFEM solution for the

simulation of HM-coupled hydro-frac-induced fracture propagation is presented and verified by comparing the results with existing analytical solutions. The equations of equilibrium and fluid continuity are separately developed and then discretized. A new method is then applied for the fluid-solid coupling to follow fracture aperture and propagation. As far as the coupling processes are concerned, two distinct algorithms are proposed, the first for the transfer of the fluid pressures inside a fracture to the surrounding medium, and the second for the evolution of fracture apertures. The solution is extended to multiple fractures and applied to study the relative interaction.

It is to remark that the proposed solution is elastic and plane strain and as such the applicability is limited to specific, albeit quite frequent, situations. As previously mentioned, hydraulic fractures usually propagate along the direction perpendicular to the minimum in situ stress (which is usually horizontal) , and therefore vertically from the borehole. When the fracture height (measured along the vertical) is sizable and remains more or less constant, and the fluid pressure and aperture/aperture slightly change along it, plane strain conditions can be considered (analysing the horizontal section).

In unconventional reservoirs, the rock mass is usually compacted and tight with very low permeability, for which visco-plastic strains are negligible and a linearly elastic medium can be assumed. In addition, rock formations of unconventional reservoirs (such as shales), may be transversely isotropic, with the plane of isotropy coinciding with the bedding; if the crack develops normally to the plane of isotropy, only the toughness (or tensile strength) along that plane is of importance and the material can be considered isotropic in the simulation and the proposed solution is applicable. For any other situation, other solutions must be adopted; even though the proposed solution may be still used in a preliminary stage. Note that the algorithms of the solution are for the simulation of fracture propagation, therefore, fracture initiation is not considered.

Throughout the text, especially when dealing with Fracture Mechanics (FM) concepts, the term crack is sometimes used as synonym of fracture.

In Table 1, a glossary of terms is reported.

2 | GOVERNING EQUATIONS

It is assumed herein that the whole hydro-frac process occurs in an isotropic linear elastic (ILE) impervious medium under plane strain conditions. A fracturing fluid at high pressure is injected at a constant volumetric rate into a borehole to promote the initiation and propagation of artificial fractures. The evolution of the propagation is regarded as a quasi-static process.

2.1 | Equilibrium equation

With reference to Figure 1, for a two-dimensional domain Ω, externally bounded by Γ with normal $\mathbf{n}$, without body forces, the equilibrium equation is

$$\nabla \cdot \boldsymbol{\sigma} = 0 \tag{1}$$

where $\boldsymbol{\sigma}$ is the stress tensor. A fluid is injected into a fracture. The following boundary conditions apply:

$$\boldsymbol{\sigma} \cdot \mathbf{n} = \mathbf{t} \qquad (\text{on} \quad \Gamma_{\mathbf{t}}) \tag{2}$$

$$\mathbf{u} = \overline{\mathbf{u}} \qquad (\text{on} \quad \Gamma_{\mathbf{u}}) \tag{3}$$

$$\boldsymbol{\sigma} \cdot \mathbf{n}_{\mathrm{f}} = -p\mathbf{n}_{\mathrm{f}+} \qquad (\text{on} \quad \Gamma_{\mathrm{f}+}) \tag{4}$$

$$\boldsymbol{\sigma} \cdot \mathbf{n}_{\mathrm{f}} = -p\mathbf{n}_{\mathrm{f}-} \quad (\text{on} \quad \Gamma_{\mathrm{f}-}) \tag{5}$$

where $\mathbf{t}$ is the vector of the boundary tractions, prescribed on $\Gamma_{\mathbf{t}}$, $\mathbf{u}$ is the vector of the displacements, $\overline{\mathbf{u}}$ is the vector of the prescribed displacements on $\Gamma_{\mathbf{u}}$, $\mathbf{n}_{\mathrm{f}+}$, $\mathbf{n}_{\mathrm{f}-}$ are the normal vectors of the fracture positive ($\Gamma_{\mathrm{f}+}$) and negative ($\Gamma_{\mathrm{f}-}$) faces, respectively, and p is the hydro-fracinduced fluid pressure in the fracture. It is also $\Gamma = \Gamma_{\mathbf{t}} \bigcup \Gamma_{\mathbf{u}}$.

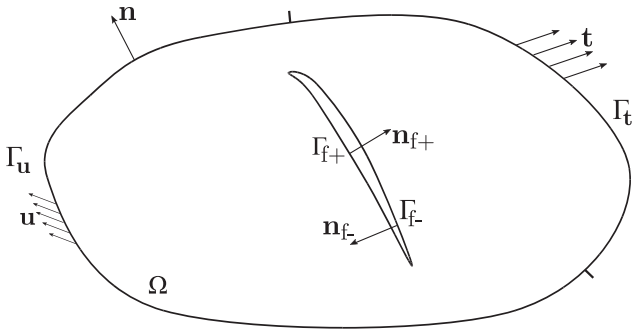

FIGURE 1 A two-dimensional domain dense of an ILE medium and a fracture. ILE, isotropic linear elastic.

A weak formulation of Equation (1) is as follows[33]:

$$\int_{\Omega} \boldsymbol{\sigma} : \boldsymbol{\varepsilon}(\mathbf{u}) \mathrm{d}\Omega = \int_{\Gamma_t} \mathbf{t} \cdot \mathbf{u} \mathrm{d}\Gamma - \int_{\Gamma_{f+}} p\mathbf{n}_{f+} \cdot \mathbf{u}_{f+} \mathrm{d}\Gamma - \int_{\Gamma_{f-}} p\mathbf{n}_{f-} \cdot \mathbf{u}_{f-} \mathrm{d}\Gamma \tag{6}$$

where $\boldsymbol{\epsilon}$ is the strain tensor, $\mathbf{u}_{f+}$, $\mathbf{u}_{f-}$ are the displacements of the points of the fracture positive and negative faces, respectively.

2.2 | Fracture fluid continuity equation

The fluid injected in a hydro-frac process in a fracture is assumed incompressible and of constant viscosity. According to the cubic law,[34,35] by neglecting the gravity, the fluid discharge per unit fracture width q_ξ is

$$q_\xi = -\frac{e^3}{12\mu} \frac{\partial p}{\partial \xi} \tag{7}$$

where ξ is, in two dimensions, the local coordinate of the fracture, μ is the fluid dynamic viscosity and e is the fracture aperture.

By applying the fluid continuity equation,[36] one has

$$\frac{\partial e(\xi, t, l)}{\partial t} + \frac{\partial q_\xi(\xi, t, l)}{\partial \xi} = Q_0 \delta(\xi_0) \tag{8}$$

where t is time, Q_0 is the volumetric fluid source at the injection point in ξ_0 and $\delta(\xi_0)$ is the Dirac delta function.

By substituting Equation (7) into Equation (8), the lubrication equation is obtained[37,38]:

$$\frac{\partial e}{\partial t} + \frac{1}{12\mu} \frac{\partial}{\partial \xi} \left(e^3 \frac{\partial p}{\partial \xi} \right) = Q_0 \delta(\xi_0) \tag{9}$$

This equation is valid provided that the fluid flow remains laminar as the fracture propagates. Equation (9) is one-dimensional as the component of the fluid flow in the direction normal to the axis is neglected, as the aperture is small compared to the fracture length.

Equations (6) and (9) are the basis equations of the proposed XFEM solution. In the next section, the discretization of the two equations in the context of XFEM is described.

3 | DISCRETIZATION OF THE EQUATIONS

As previously stated, by resorting to XFEM, fracture propagation is modelled by avoiding re-meshing. The discontinuous displacements of the fracture walls can be efficiently represented by adding enrichment functions to the standard finite

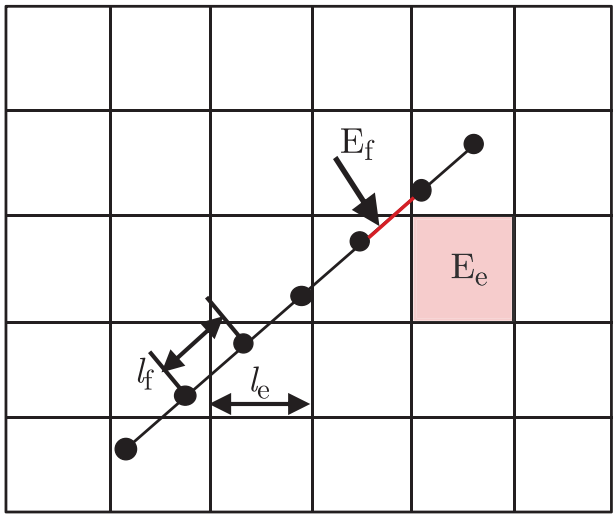

FIGURE 2 Fracture element E_f and ILE element E_e.

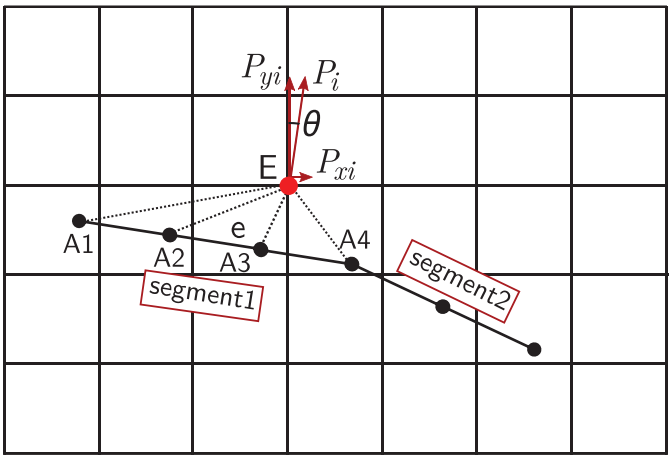

FIGURE 3 Schematic of pressure transfer from fluid-flow nodes to ILE-medium nodes. ILE, isotropic linear elastic.

element approximation. So, concerning a single fracture, the approximated solution for the displacement $\mathbf{u}$ is[39,40]:

$$\mathbf{u}=\sum_{i=1}^{N^s}N_i\mathbf{u}_i+\sum_{j=1}^{N^{cut}}N_jH[\phi(x,y)]\mathbf{a}_j+\sum_{k=1}^{N^{tip1}}N_k\left[\sum_{l1=1}^{4}\psi_{l1}^{(1)}(x,y)\mathbf{b}_k(l1)\right]+\sum_{k=1}^{N^{tip2}}N_k\left[\sum_{l2=1}^{4}\psi_{l2}^{(2)}(x,y)\mathbf{b}_k(l2)\right] \tag{10}$$

where N^s is the number of standard nodes, N_i are the standard shape functions, $\mathbf{u}_i$ is the vector of nodal displacements, N^{cut} is the number of enriched nodes of the elements crossed by the fracture, $H[\phi(x,y)]$ is the jump function[41]:

$$H[\phi(x,y)]=\begin{cases}+1 & \phi(x,y)>0\\ -1 & \phi(x,y)<0\end{cases} \tag{11}$$

with $\phi(x,y)$ the signed distance function, N^{tip1}, N^{tip2} are the numbers of enriched nodes of the first crack tip and the second crack tip, respectively, $\psi_l^{(1)}$ and $\psi_l^{(2)}$ are the tip branch functions at the first and the second crack tips, respectively, that can be written using polar coordinates r,θ with origin at the respective crack tips as follows[42,43]:

$$\{\psi_l(r,\theta)\}_{l=1}^4=\left[\sqrt{r}\sin\frac{\theta}{2},\sqrt{r}\sin\frac{\theta}{2}\sin\theta,\sqrt{r}\cos\frac{\theta}{2},\sqrt{r}\cos\frac{\theta}{2}\sin\theta\right] \tag{12}$$

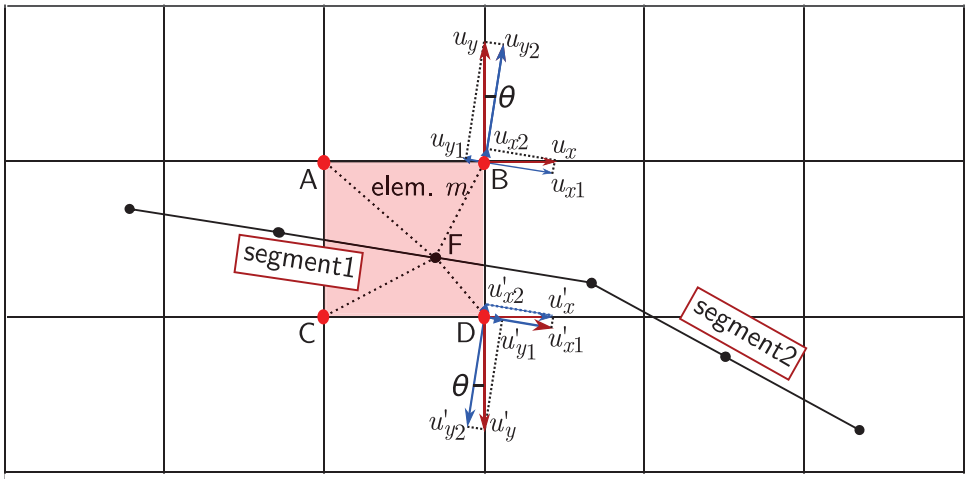

FIGURE 4 Displacements around a fracture for the aperture change.

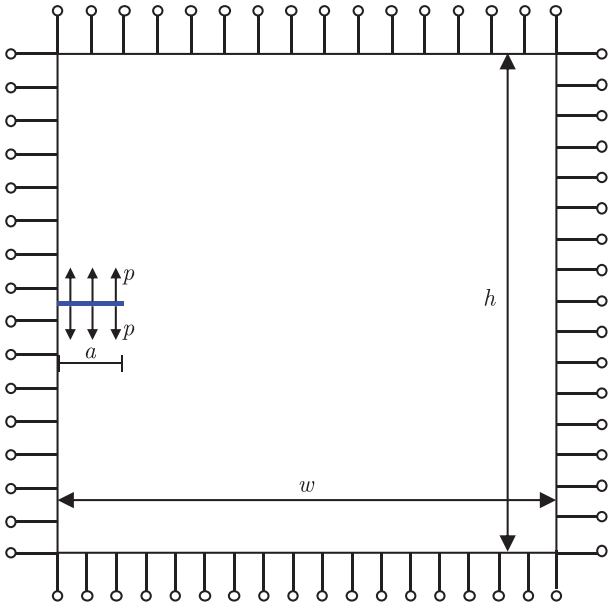

FIGURE 5 Schematic of a single hydraulic fracture in an elastic domain.

and, finally, **a** and **b** are the additional degrees of freedom (dofs) for the enriched nodes. By using the tip branch functions ψ, the convergence of the numerical solution is faster. By substituting Equation (10) into Equation (6), the following compact form of the discretized governing equation for stress/strain is obtained:

$$\mathbf{Ku} = \mathbf{P} \tag{13}$$

where **K** is the global stiffness matrix, **u** is the nodal displacement vector and **P** is the force vector, condensing the contributions of the external tractions and the tractions at the fracture faces. Matrix **K** is as follows:

$$\mathbf{K} = \int_{\Omega} \mathbf{B}^{\mathrm{T}}\mathbf{DB}\mathrm{d}\Omega \tag{14}$$

in which **D** is the matrix of the elasticity coefficients, and **B** is the strain differential operator matrix, containing the derivatives of the shape and enrichment functions.

For node i, the strain differential operator matrix for the Heaviside enrichment is

$$\mathbf{B}_i^{\mathbf{a}} = \begin{bmatrix} [N_i(H-H_i)]_{,x} & 0 \\ 0 & [N_i(H-H_i)]_{,y} \\ [N_i(H-H_i)]_{,y} & [N_i(H-H_i)]_{,x} \end{bmatrix} \tag{15}$$

in which H_i is the enrichment value at i; since H depends only on the sign of $\phi(x,y)$, $\mathbf{B}_i^{\mathbf{a}}$ can be transformed as follows:

$$\mathbf{B}_i^{\mathbf{a}} = \begin{bmatrix} N_{i,x}(H-H_i) & 0 \\ 0 & N_{i,y}(H-H_i) \\ N_{i,y}(H-H_i) & N_{i,x}(H-H_i) \end{bmatrix} \tag{16}$$

For the crack tip enrichment, $\mathbf{B}_i^{\mathbf{b}}$ can be expressed instead as

$$\mathbf{B}_i^{\mathbf{b}} = \begin{bmatrix} [N_i(\psi_l-\psi_{li})]_{,x} & 0 \\ 0 & [N_i(\psi_l-\psi_{li})]_{,y} \\ [N_i(\psi_l-\psi_{li})]_{,y} & [N_i(\psi_l-\psi_{li})]_{,x} \end{bmatrix}_{l=1,2,3,4} \tag{17}$$

where ψ_{li} is the tip branch function (crack tip 1 or 2) at node 1; Equation (17) can be expanded as follows:

$$\mathbf{B}_i^{\mathbf{b}} = \begin{bmatrix} N_{i,x}(\psi-\psi_{li}) + N_i(\psi-\psi_{li})_{,x} & 0 \\ 0 & N_{i,y}(\psi-\psi_{li}) + N_i(\psi-\psi_{li})_{,y} \\ N_{i,y}(\psi-\psi_{li}) + N_i(\psi-\psi_{li})_{,y} & N_{i,x}(\psi-\psi_{li}) + N_i(\psi-\psi_{li})_{,x} \end{bmatrix}_{l=1,2,3,4} \tag{18}$$

The right-hand side vector is comprised of the nodal forces due to the external tractions and fluid pressures on the fracture faces and consists of a contribution $\mathbf{P}^{\text{st}}$ of the standard nodes and a contribution $\mathbf{P}^{\text{en}}$ of the enriched nodes:

$$\mathbf{P} = \begin{Bmatrix} \mathbf{P}^{\text{st}} \\ \mathbf{P}^{\text{en}} \end{Bmatrix} \tag{19}$$

3.1 | Fluid continuity equation

The fracture apertures increase as long as the fracture propagates and the frac-fluid is injected into the borehole. For the one-dimensional fluid continuity equation, that is, Equation (9), the fracture can be subdivided into one-dimensional linear elements (E_{f} in Figure 2). In order to lower the complexity of the calculations, such elements have the same length of the edges of the finite elements used to discretise the domain (equal-size square elements E_{e} in Figure 2). However, the fracture nodes of Equation (9) (*fluid-flow* nodes) do not necessarily coincide with the nodes of the domain (*ILE-medium* nodes). The fluid pressures are transformed into nodal forces applied on the ILE-medium nodes and the local fracture apertures are calculated according to the nodal displacements of the two corresponding points of the fracture.

A backward difference can be used for the fracture aperture e:

$$\frac{\partial e}{\partial t} = \frac{e^n - e^{n-1}}{\Delta t} \tag{20}$$

where Δt is the time increment for the nth time step. By using Equation (20), Equation (9) for node k of a fracture can be written as

$$\frac{e_k^n - e_k^{n-1}}{\Delta t} = -\frac{1}{12\mu}\frac{\partial}{\partial \xi}\left[(e_k^n)^3 \frac{\partial p_k^n}{\partial \xi}\right] + Q_0\delta(\xi_0) \tag{21}$$

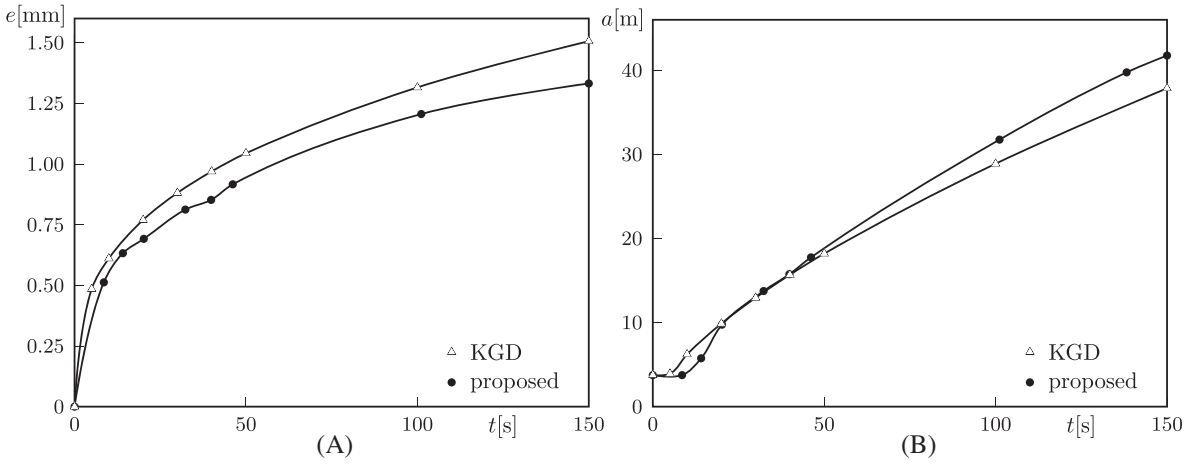

FIGURE 6 Example 1; comparison between the KGD analytical solution and the proposed solution; (A) maximum aperture e versus time t; (B) fracture half-length a versus time t. KGD, Khristianovic–Geertsma–de Klerk.

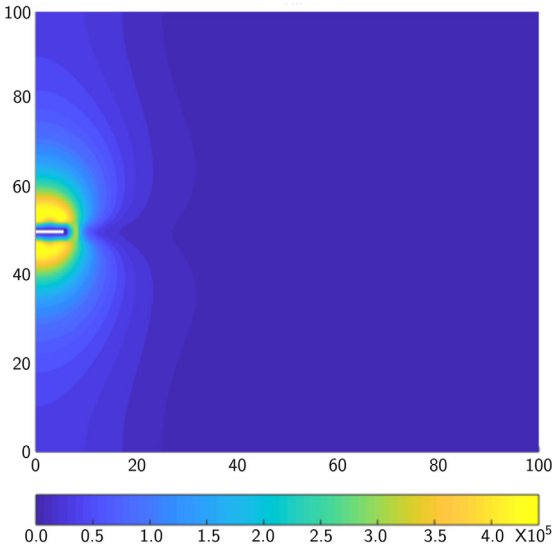

FIGURE 7 Example 1: contour plot of the von Mises stress σ_{vm} [Pa].

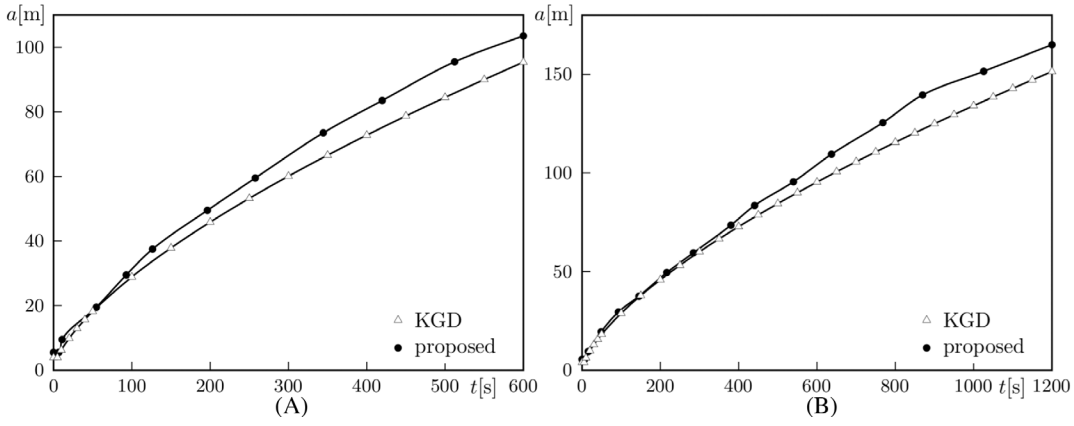

FIGURE 8 Example 1; comparison between the KGD analytical solution and the proposed solution for the evolution of the fracture half-length with time t for (A) 200 × 200-m^2 domain, and (B) 300 × 300-m^2 domain. KGD, Khristianovic–Geertsma–de Klerk.

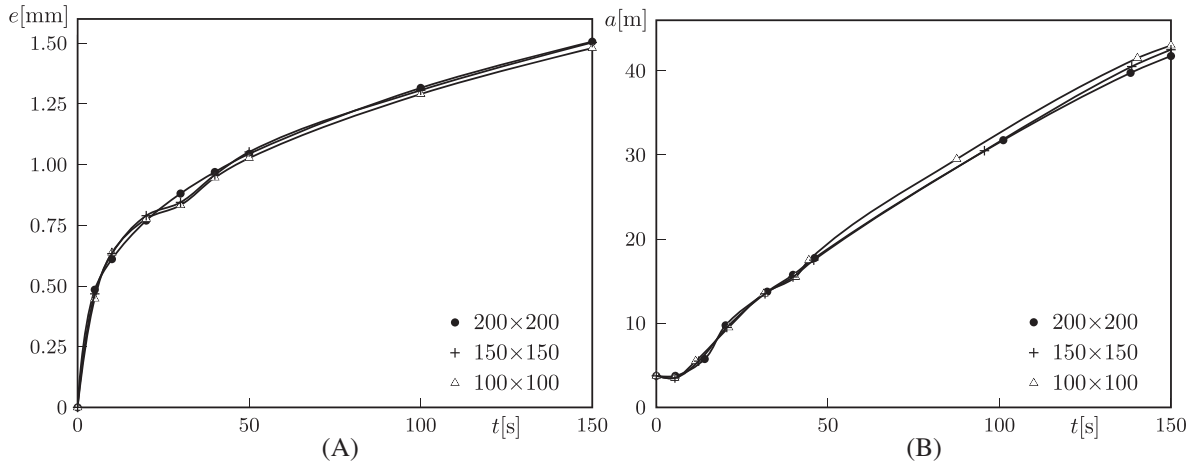

FIGURE 9 Example 1; sensitivity analysis of the solution to the element size for the discretizations 100×100, 150×150, 200×200; (A) maximum aperture e versus time t; (B) half-length a versus time t.

4 | COUPLING OF THE EQUATIONS

The injection of the frac-fluid leads to both the fracture propagation and the increase of the fracture aperture. The stress/strain regime in the rock is influenced by the pressure distribution in a propagating fracture. As previously mentioned, the interaction between body and fracture is a HM-coupled process, whose governing equations are Equations (6) and (9). By considering the corresponding discretized versions, the HM-coupled process can be, therefore, simulated by solving the following system of equations:

$$\begin{cases} \mathbf{K}\mathbf{u} = \mathbf{P} \\ \dfrac{\partial e}{\partial t} + \dfrac{1}{12\mu}\dfrac{\partial}{\partial \xi}\left(e^3 \dfrac{\partial p}{\partial \xi}\right) = Q_0 \delta(\xi_0) \end{cases} \tag{22}$$

where the nodal displacements $\mathbf{u}$, and fluid pressures p are the unknowns. The terms of the vector $\mathbf{P}$ (due to the boundary conditions at the fracture faces) of the first equation depend on the values of p from the second equation. In turn, the nodal aperture depends on $\mathbf{u}$. As the nodes of the discretizations of the two equations do not coincide, two methods are proposed herein, the first for the transfer of fluid pressure to the ILE medium, the second for adjusting the fracture aperture with the displacements; using both methods together, errors are minimised.

4.1 | Transfer of the fluid pressures to the ILE medium

The first step of the HM-coupled process is to set an initial value for the fluid pressure, acting on the two faces of the fracture. In general, the fluid pressures along the fracture are transformed into nodal forces on the mesh elements. Given that, as previously mentioned, fluid-flow nodes and ILE-medium nodes do not necessarily coincide; for the transfer of such pressure values, an expedient is required. If the mesh is fine, the distance between a fluid-flow node and a corresponding ILE-medium node (in the direction normal to the fracture) is presumably small, therefore, the pressure value can be directly ascribed to the ILE-medium node. In this respect, finding the correspondence between nodes is an important step to gain a good accuracy of the solution. The proposed method is based on the principle of proximity and is illustrated by resorting to an example.

With reference to Figure 3, an ILE-medium node is used as a landmark (node E); the nearest fluid-flow node is then regarded as a pairing node transferring pressure (in terms of nodal force) to this landmark node. The distances d_i from E to the surrounding fluid-flow nodes A_1, A_2, A_3, A_4 are

$$d_i = \left\{ \sqrt{(x_i - x_E)^2 + (y_i - y_E)^2} \right\}_{i=A_1,A_2,A_3,A_4} \tag{23}$$

Node A_3 is the nearest node to E (d_{A_3} is the minimum value among d_i), hence A_3 and E are the pairing nodes, so the pressure of A_3 will be assigned to node E.

The nodal force P_i corresponding to the fluid pressure p_i (normal to the fracture face) is then decomposed into x and y components, contributing to the right-hand side vector of Equation (13):

$$\begin{cases} P_{x_i} = P_i \sin\theta \\ P_{y_i} = P_i \cos\theta \end{cases} \tag{24}$$

where θ is the angle between the fracture segment and x. It is worth noting that the fluid pressure is applied to both standard nodes and enriched nodes.

4.2 | Evolution of the fracture aperture

By transferring the fluid pressures to the elastic body, Equation (13) can be solved and the nodal displacements can be obtained, thus the new value of the fracture aperture can be derived by summing the offsets of the two fracture faces in Equation (21); the aperture e_k^n at time step n can be approximately represented by the sum of displacements of the two corresponding ILE-medium nodes on the two fracture faces when the domain is finely meshed. The four ILE-medium nodes of a fracture-sectioned element are usually divided into two sets, one for each portion of the element. From each set, the nearest node to the fluid-flow node is selected, whose displacement is considered as the one-wing displacement of the same fluid-flow node.

In what follows, the process for calculating the aperture change is illustrated through the example of Figure 4, where a fluid-flow node F is located in mesh element m and two sets of nodes are defined pertaining to the two portions in which m is sectioned by the fracture (positive and negative by considering the normal $\mathbf{n}_{f+}$, in this case, the positive set is above, the negative below the fracture). Nodes A and B pertain to the set above, and nodes C and D to the set below. The distances d_i from the four ILE-medium nodes to the fluid-flow node are

$$d_i = \left\{ \sqrt{(x_i - x_F)^2 + (y_i - y_F)^2} \right\}_{i=A,B,C,D} \tag{25}$$

In Figure 4, by comparing the values of d_i, it can be concluded that node B has the minimum distance to node F for the set above the fracture and node D has the minimum distance to node F for the set below the fracture.

Thus, nodes B and D are used on the two wings to calculate the aperture change. The sum of the displacements in two opposite directions is considered as the overall aperture of node F. With reference to Figure 4, u_x and u_y are the node-B displacement components along the x-axis and y-axis, respectively; the component u_x can be further decomposed into components u_{x_1}, u_{x_2}, parallel and normal to the fracture segment, respectively, as follows:

$$\begin{cases} u_{x_1} = u_x \cos\theta \\ u_{x_2} = u_x \sin\theta \end{cases} \tag{26}$$

Similarly, u_y can be decomposed into u_{y_1}, u_{y_2}, parallel and normal to the fracture segment, respectively:

$$\begin{cases} u_{y_1} = u_y \sin\theta \\ u_{y_2} = u_y \cos\theta \end{cases} \tag{27}$$

Finally, the one-wing aperture change of node B is

$$\Delta e^+ = u_{x_2} + u_{y_2} \tag{28}$$

The aperture change Δe^- of node D can be similarly obtained (quantities with prime in Figure 4 refer to node D). The total aperture change Δe at node F can be expressed as

$$\Delta e = \Delta e^+ + \Delta e^- \tag{29}$$

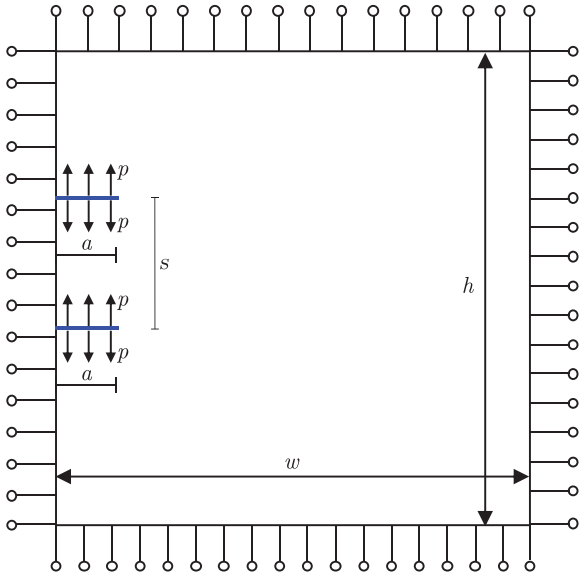

FIGURE 10 Schematic of Example 2 first scheme with two parallel hydraulic fractures.

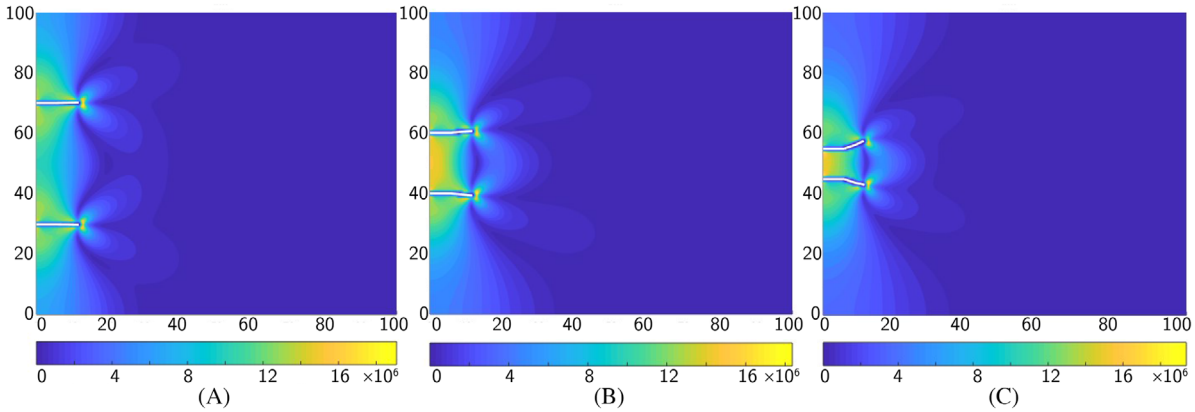

FIGURE 11 Example 2 first scheme (two parallel fractures): contour plots of the von Mises stress σ_{vm} [Pa] and propagation trajectories (up to 10 m) for spacing s 40 m (A), 20 m (B) and 10 m (C).

Equation (29) is an approximate solution for the fracture aperture, whose errors can be reduced by optimising the mesh size to shrink the gap between the fluid-flow and the ILE-medium nodes. A study of the sensitivity of the results to the mesh size is reported in the next section.

5 | THE NUMERICAL SOLUTION

As previously described, the HM-coupled response in a hydro-frac process can be numerically simulated by resorting to Equation (22). For the solution of such a system, an iterative procedure within each time step is required; it is explained in what follows.

5.1 | Iterative process

The aperture in Equation (29) can be substituted into Equation (21) to obtain the updated fluid pressure value, which, in turn, can be substituted back into Equation (13) to obtain the nodal displacements. This leads to an iterative procedure. The Picard method is employed to facilitate the convergence of the coupling equations.

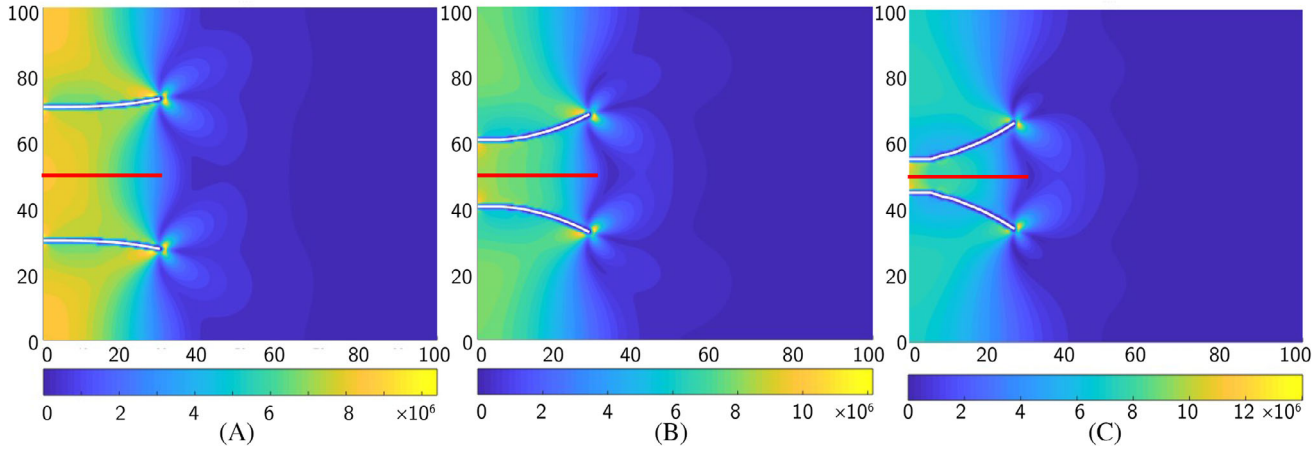

FIGURE 12 Example 2 first scheme (two parallel fractures): contour plots of the von Mises stress σ_{vm} [Pa] and extended propagation trajectories (up to 30 m) for spacing s 40 m (A), 20 m (B) and 10 m (C).

The length of fracture propagation at each time step is set, so the time step can be determined according to propagation length and aperture. As the fracture continuously propagates and widens, the time increment at each time step n can be calculated as

$$\Delta t = \frac{1}{Q_0}\left[\sum_i^{N_f} e_i^n - \sum_i^{N_f} e_i^{n-1}\right] \tag{30}$$

where e_i are the nodal aperture values and N_f is the number of the nodes of the fracture. With reference to a single fracture, the procedure is as follows:

1. an initial fluid pressure p_i^0 is applied to all the fracture nodes in Equation (13) to calculate the displacements; then, through Equations (25)–(29), new aperture values e_i^1 are obtained;
2. the e_i^1 values are then substituted into Equation (21) to obtain new fluid pressure values p_i^1, to be inserted in Equation (13);
3. steps 1 and 2 are repeated until the following convergence criterion is met:

$$\frac{\sum_i^{N_f}\left|p_i^{n+1} - p_i^n\right|}{\sum_i^{N_f}\left|p_i^n\right|} \leq \mathrm{TOL} \tag{31}$$

where TOL is a tolerance;

4. if the convergence criterion (31) is not met, the pressure values are adjusted as follows:

$$p_i^{n+1,j} = p_i^n + \alpha p_i^{n+1,j-1} \tag{32}$$

where j is the iteration number and α is between 0 and 0.5.

5.2 | Propagation criterion

The fluid pressure near the crack tip usually decreases sharply to zero, so the fluid lag region near the crack tip is regarded as a small area. This region has little effect on the propagation, therefore, it is assumed that the fluid front coincides with the crack front. In the context of FM, for the crack propagation, the maximum circumferential stress criterion[44] is used to determine the potential propagation direction. Withthe criterion, the propagation occurs if the current stress intensity

factor (SIF) equates to the corresponding critical value K_c. The effective SIF is derived as follows[45]:

$$dK = \left(K_1^4 + 8K_2^4\right)^{1/4} \tag{33}$$

where K_1 and K_2 are the SIF values near the crack tip for Mode-I and Mode-II, respectively. If the effective SIF is larger than the critical SIF, the crack will propagate along the maximum circumferential stress direction. In addition, the crack kink angle is[46]

$$\theta = 2\arctan\left[\frac{1}{4}\left(\frac{K_1}{K_2} \pm \sqrt{\left(\frac{K_1}{K_2}\right)^2 + 8}\right)\right] \tag{34}$$

To calculate the SIF values, several methods are available in the literature.[47–53] In this paper, the interaction integral method is adopted; it is based on the J integral by resorting to an auxiliary stress field.

In what follows, the results of some examples are illustrated to show the validity of the proposed numerical method, implemented in a Matlab code. The results are used to examine the sensitivity of the propagation and interaction of multiple hydraulic fractures to the parameters of the problem.

6 | NUMERICAL EXAMPLES

6.1 | Example 1: Single hydraulic fracture

With reference to Figure 5, a single hydraulic fracture subjected to fluid pressure produced by hydro-frac operations is considered. The properties of the elastic medium include Young's modulus E 39.5 GPa and Poisson's ratio ν 0.3. The fluid pressure inside the fracture is regarded as net pressure, so the in situ stress can be ignored. The fluid has a viscosity μ equal to 10 mPa·s and the injection rate Q_0 is 0.00028 m^3/s. An injection time of 150 s is assumed.

The simulation domain $w \times h$ is 100 × 100 m^2. A horizontal fracture (initial half-length a=3.5 m) is located in the middle of the domain originating from the left vertical boundary (that is also a symmetry plane). Equal-size four-node quadrilateral elements are employed for the mesh. The displacements along the normal to the boundaries are zero. The injection pressure is applied in the fracture at the left vertical boundary.

The results furnished by the numerical code are compared with the corresponding analytical solution in terms of fracture aperture e (the maximum value) and half-length a as a function of time (Figure 6A,B). In addition, the contour plot of the von Mises stress σ_{vm} is shown in Figure 7. For the first half of the injection time, the results of the code are in good agreement with the analytical solution, whereas, for the second half, a difference between the two solutions emerges. It should be noted that the KGD solution is for an infinite domain; therefore, the proposed numerical solution differs due to the effect of the boundary conditions. Such an effect is more pronounced and the discrepancy expands as the fracture tip approaches the boundaries, or, with reference to the example, with the increase of the ratio a/w. To prove this claim, the simulation is extended to 200 × 200 m^2 and 300 × 300 m^2 domains, maintaining the element size and the initial fracture length a. The results in terms of a, plotted against time, are reported in Figure 8A,B, respectively. Again, like for the simulation with the 100 × 100m^2 domain, the numerical solution is in good agreement with the corresponding analytical solution at the initial stages (note that the injection time is longer than for the 100 × 100m^2 domain), whereas, at later times, the numerical solution diverges as the fracture propagates. It is, therefore, apparent that, for the boundary conditions imposed at the edges (fixed boundaries), such a discrepancy always substantiates.

Finally, to study the sensitivity of the solution to the element size, three meshes are investigated (100 × 100, 150 × 150, and 200 × 200 elements) and the results in terms of maximum aperture and half-length are compared (Figure 9A,B). One can notice that by reducing element size (refining the mesh), no significant improvement is gained.

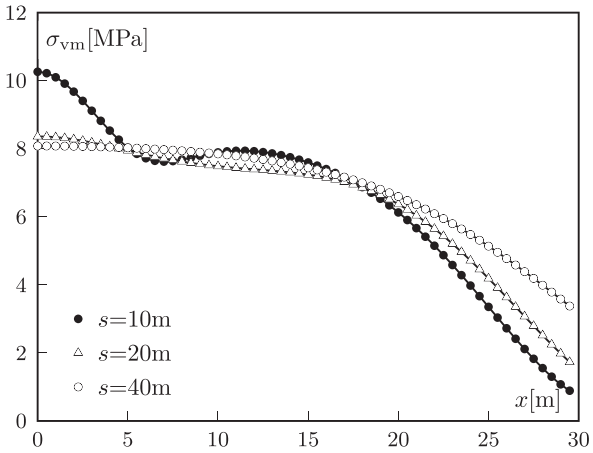

FIGURE 13 Example 2 first scheme (two parallel fractures): distributions of von Mises stress σ_{vm} along the middle (red) lines of Figure 12 for spacing s 10, 20 and 40 m.

6.2 | Example 2: Multiple fractures

In what follows, the results of the application of the numerical solution to schemes with multiple initial fractures are described. The equation system (22) is purposely modified as follows:

$$\begin{cases} \begin{bmatrix} \mathbf{K}_{st} & \sum_{\nu_f} \mathbf{K}_{st,en} \\ \sum_{\nu_f} \mathbf{K}_{en,st} & \sum_{\nu_f} \mathbf{K}_{en} \end{bmatrix} \begin{bmatrix} \mathbf{u}_{st} \\ \sum_{\nu_f} \mathbf{u}_{en} \end{bmatrix} = \begin{bmatrix} \mathbf{P}_{st} \\ \sum_{\nu_f} \mathbf{P}_{en} \end{bmatrix} \\ \frac{\partial e}{\partial t} + \frac{1}{12\mu} \frac{\partial}{\partial \xi} \left(e^3 \frac{\partial P}{\partial \xi} \right) = Q_0 \delta(\xi_0), \qquad \forall \text{frac.} \end{cases} \tag{35}$$

where ν_f is the number of fractures, $\mathbf{K}_{st}$ is the standard stiffness matrix, $\mathbf{K}_{en}$ is the enriched stiffness matrix and $\mathbf{K}_{st,en}$, $\mathbf{K}_{en,st}$ the cross matrices.

Mesh and material properties of Example 1 are also adopted here. The fractures are assumed horizontal and have an initial half-length (a =3.5m). A sensitivity analysis of the fracture growth trajectories to the fracture spacing is performed in what follows.

In a first scheme, with reference to Figure 10, two fractures are symmetrically set with respect to the middle horizontal line. For the sensitivity analysis, three spacing values s are considered: 40, 20, and 10 m. The contour plots of the von Mises stress σ_{vm} are shown in Figure 11 for a propagation length of 10 m. For s equal to 40 m, the propagation trajectories are subjected to a slight deflection (Figure 11A), whereas, for the other two cases, the deflection is more pronounced and the trajectories diverge as a consequence of the interaction among the fractures, resulting in a repelling effect (Figure 11B,C). Similar considerations can be drawn for the extended propagation (up to a total length of 30 m for both fractures). In Figure 12A–C, it is shown that for the largest spacing, the two fractures propagate nearly in parallel (no mutual interaction), while for the other cases, due to the repelling effect, the propagation trajectories consistently diverge.

Another effect of the interaction among propagating fractures is the shadow effect, reflected in the stress variations along the propagation paths, as shown in Figure 13, where the change of von Mises stress σ_{vm} is plotted against the horizontal distance from the injection along the line in the middle of the two fractures (the red lines in Figure 12) for the three cases of first scheme. It can be seen that σ_{vm} for s 10 m has a sharp decrease corresponding to the diverging of the fractures, whereas, for s 40 m, σ_{vm} is uniform up to 20 m from the injection. A moderate stress interference is experienced for s 20 m.

In a second scheme, the number of hydraulic fractures is increased to three by adding a horizontal fracture aligned along the middle horizontal line (see Figure 14) with three different mutual spacing s 20, 10 and 5 m. The results of the simulation in terms of contour plots of σ_{vm} are shown in Figure 15 for a propagation length of 10 m, and in Figure 16 for a propagation length of 30 m. With the introduction of the middle fracture, by the decreasing of the spacing, the repelling

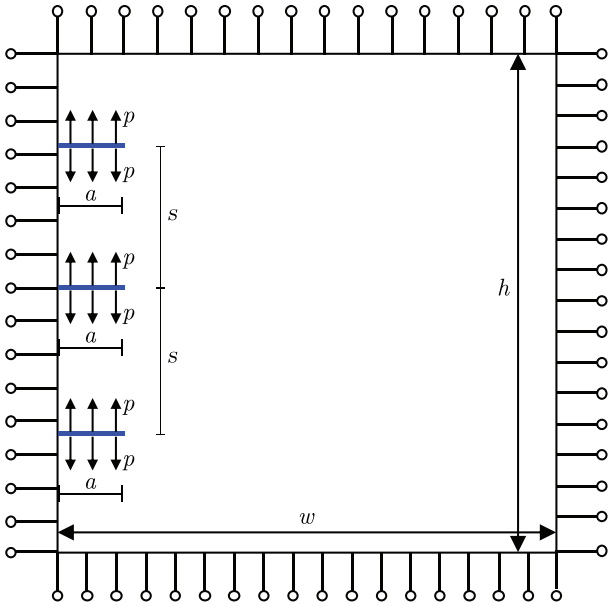

FIGURE 14 Schematic of Example 2 second scheme with three parallel hydraulic fractures.

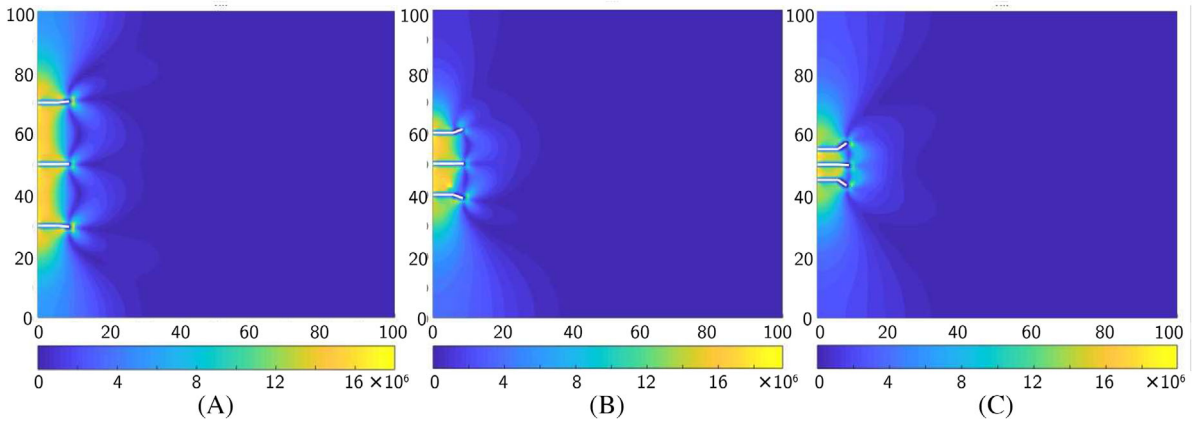

FIGURE 15 Example 2 second scheme (three parallel fractures): contour plots of the von Mises stress σ_{vm} [Pa] and propagation trajectories (up to 10 m) for spacing s 20 m (A), 10 m (B), and 5 m (C).

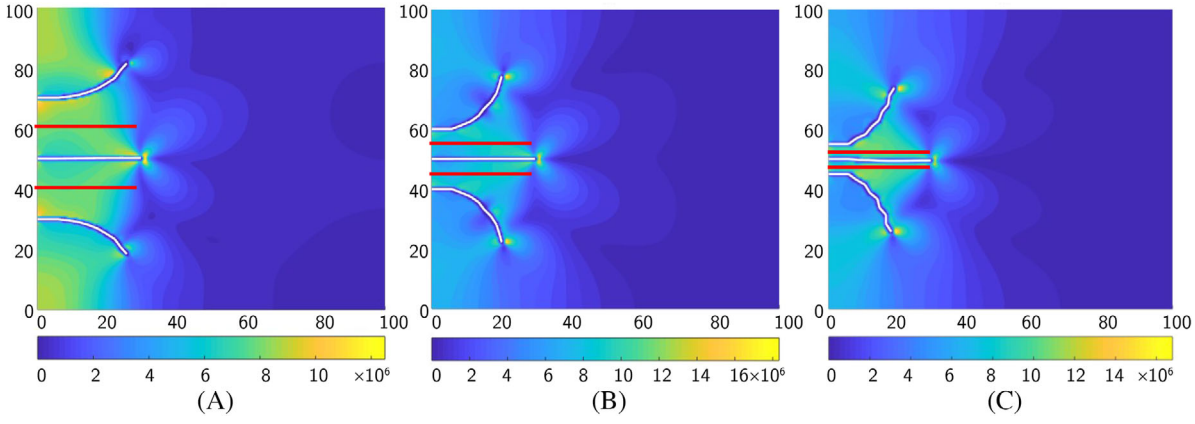

FIGURE 16 Example 2 second scheme (three parallel fractures): contour plots of the von Mises stress σ_{vm} [Pa] and extended propagation trajectories (up to 30 m) for spacing s 20 m (A), 10 m (B) and 5 m (C).

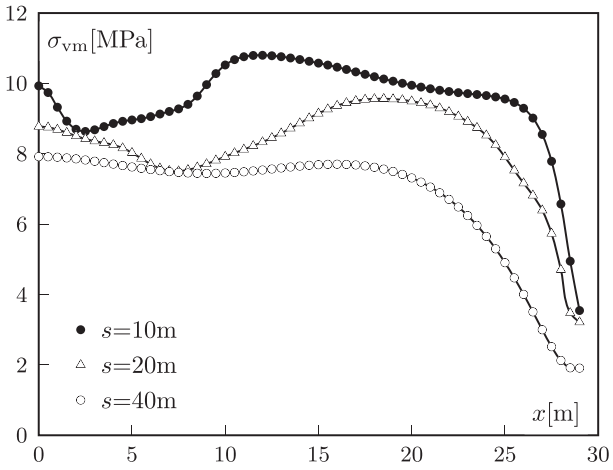

FIGURE 17 Example 2 second scheme (three parallel fractures): distributions of von Mises stress σ_{vm} along the middle (red) lines of Figure 16 for spacing s 5, 10 and 20 m.

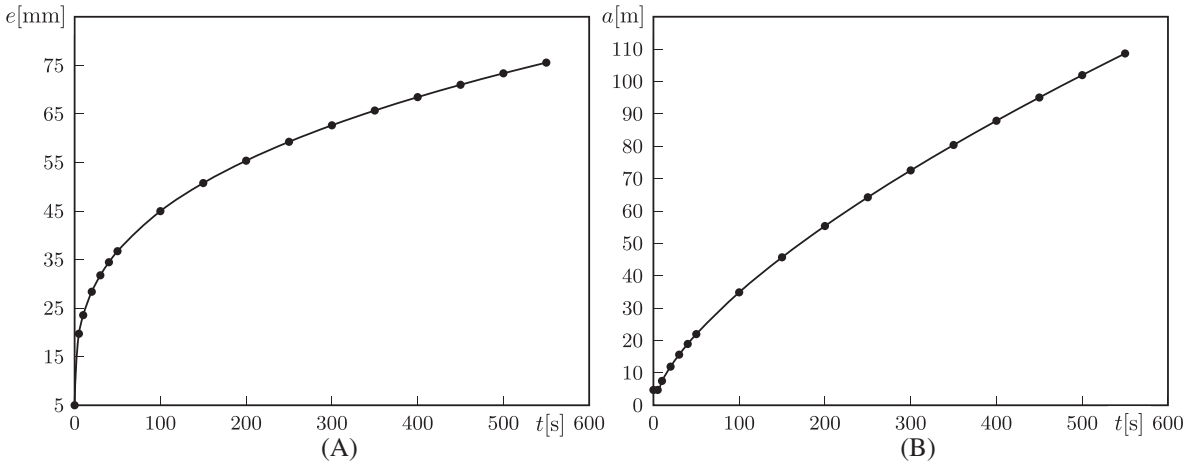

FIGURE 18 Maximum aperture and half-length versus time for viscosity μ 2.39 Pa·s.

effect among fractures is enhanced, leading to even larger deflections. Note that the stress concentrations around the crack tips connect to form an intensified stress band, thus explaining the strong repelling effect.

To show the shadow effect for this scheme, the σ_{vm} values along the middle lines between the fractures (the red segments in Figure 16A–C) are plotted against the distance from the injection point. As shown in Figure 17, for all the cases, the distributions are characterised by a decreasing trend in the initial stage, followed by an increasing trend in the middle stage (presumably caused by the deflection of the side-crack trajectory, leading to stress concentration), and, finally, by a sharp decrease in the last stage, once the side cracks substantially divert from the middle crack.

6.3 | Application example

To verify the effectiveness, the proposed solution is applied to a real case, previously documented in the literature.[25] The fluid injection rate is 0.11 m^3. The rock has Young's modulus E 600 MPa and Poisson's ratio ν 0.3. The fracture fluid is seen as a Newtonian fluid with a viscosity μ 2.39 Pa·s. The injection time lasts 9 min. Substituting those parameters into the code, the results of maximum aperture e and half-length a are plotted against time in Figure 18A,B. Note that the values of e and a are slightly larger than in the original document because herein the fluid viscosity is assumed constant with the pressure.

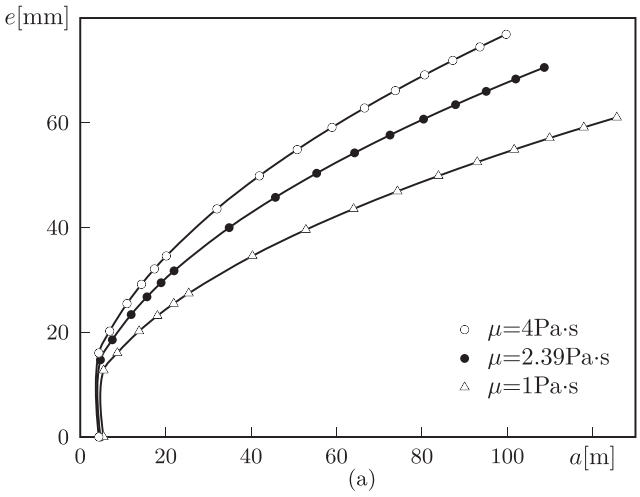

FIGURE 19 Maximum aperture versus half-length for different viscosity values (μ 1, 2.39, 4 Pa·s).

The objective of the simulation is also to check the sensitivity of fracture propagation and opening to the fluid viscosity μ. Therefore, three values of μ are considered (1, 2.39, 4 Pa·s) for comparison. The results are reported in Figure 19. As expected, higher viscosity values lead to extended propagation and opening. Such tendencies are well captured by the proposed numerical solution.

7 | CONCLUSION

In this paper, an HM-coupled solution is proposed for the prediction of the hydro-frac process in 2D schemes, combining the fluid continuity equation for the propagating fractures and the equilibrium equation for the rock. The relative numerical discretization has been performed by resorting to XFEM. The temporal derivatives are handled by using a finite differences scheme. For the quality of the results, the transfer of variables between the equations is crucial. Herein, the nodes pertaining to the two discretizations are practically forced to coincide.

With reference to a fluid injection in a single fracture, the proposed solution is validated by comparing it with an analytical solution inan infinite domain. Apart from the slight difference at later stages of the simulation, presumably due to the effect of the finite domain and boundary conditions, the two solutions match quite well.

The interaction of multiple hydraulic fractures is also studied. A sensitivity analysis of the propagation geometry to fracture spacing is proposed. It can be stated that the spacing between the fractures has a significant effect on the propagation direction. The shadow effect between multiple cracks is also illustrated by means of the stress curves along the fracture propagation paths, to show the influence of the shadow effect as fracture propagates.

Finally, the solution of an application example is provided; the sensitivity of the viscosity values in terms of maximum aperture and half-length of the considered fracture is also shown.

DATA AVAILABILITY STATEMENT

Data sharing not applicable, no new data generated or the article describes entirely theoretical research.

ORCID

Yuxiao Wang https://orcid.org/0000-0003-1770-4277
Akbar A. Javadi https://orcid.org/0000-0001-8376-4652

REFERENCES

1. Vengosh A, Warner N, Jackson R, Darrah T. The effects of shale gas exploration and hydraulic fracturing on the quality of water resources in the United States. *Procedia Earth Planet Sci*. 2013;7:863-866.
2. EIA U. United States Energy Information Administration. 2013. *Annual Energy Outlook*. 2013.

3. Geertsma J, De Klerk F. A rapid method of predicting width and extent of hydraulically induced fractures. *J Pet Technol*. 1969;21(12):1571-1581. https://doi.org/10.2118/2458-PA
4. Khristianovich S, Zheltov V. Formation of vertical fractures by means of highly viscous liquid. In: Proceedings of the 4th World Petroleum Congress. WPC; 1955:6-15.
5. Perkins T, Kern L. Widths of hydraulic fractures. *J Pet Technol*. 1961;13(09):937-949. https://doi.org/10.2118/89-PA
6. Nordgren R. Propagation of a vertical hydraulic fracture. *Soc Pet Eng J*. 1972;12(04):306-314. https://doi.org/10.2118/3009-PA
7. Hubbert M, Willis D. Mechanics of hydraulic fracturing. *Trans Soc Pet Eng AIME*. 1957;210(1):153-168.
8. Clifton R, Abou-Sayed A. A variational approach to the prediction of the three-dimensional geometry of hydraulic fractures. In: Proceedings of the SPE Rocky Mountain Petroleum Technology Conference & Low Permeability Reservoirs Symposium. SPE; 1981. SPE-9879-MS.
9. Abou-Sayed A, Sinha K, Clifton R. Evaluation of the influence of in-situ reservoir conditions on the geometry of hydraulic fractures using a 3-D simulator: part 1 – technical approach. In: Proceedings of the SPE Unconventional Resources Conference & Gas Technology Symposium. SPE; 1984.
10. Abass H, Hedayati S, Meadows D. Nonplanar fracture propagation from a horizontal wellbore: experimental study. *SPE Prod Facil*. 1996;11(03):133-137. https://doi.org/10.2118/24823-PA
11. Ma X, Zou Y, Li N, Chen M, Zhang Y, Liu Z. Experimental study on the mechanism of hydraulic fracture growth in a glutenite reservoir. *J Struct Geol*. 2017;97:37-47. https://doi.org/10.1016/j.jsg.2017.02.012
12. He J, Lin C, Li X, Zhang Y, Chen Y. Initiation, propagation, closure and morphology of hydraulic fractures in sandstone cores. *Fuel*. 2017;208:65-70. https://doi.org/10.1016/j.fuel.2017.06.080
13. Chitrala Y, Moreno C, Sondergeld C, Rai C. An experimental investigation into hydraulic fracture propagation under different applied stresses in tight sands using acoustic emissions. *J Pet Sci Eng*. 2013;108:151-161. https://doi.org/10.1016/j.petrol.2013.01.002
14. Petunin V. Finite difference approach to modeling geomechanics in hydraulic fracturing. In: Proceedings of the 47th US Rock Mechanics/Geomechanics Symposium. ARMA; 2013. ARMA 13-460
15. Cheng Y. Boundary element analysis of the stress distribution around multiple fractures: implications for the spacing of perforation clusters of hydraulically fractured horizontal wells. In: SPE Eastern Regional Meeting. SPE; 2009. SPE-125769-MS
16. Ng AK, Small JC. A case study of hydraulic fracturing using finite element methods. *Can Geotech J*. 1999;36(5):861-875.
17. Khoei AR, Hirmand M, Vahab M, Bazargan M. An enriched FEM technique for modeling hydraulically driven cohesive fracture propagation in impermeable media with frictional natural faults: numerical and experimental investigations. *Int J Numer Methods Eng*. 2015;104(6):439-468.
18. Chen Z, Bunger A, Zhang X, Jeffrey R. Implicit level set schemes for modeling hydraulic fractures using the XFEM. *Acta Mech Solida Sin*. 2009;22:443-452. https://doi.org/10.1016/S0894-9166(09)60295-0
19. Mohammadnejad T, Khoei A. An extended finite element method for hydraulic fracture propagation in deformable porous media with the cohesive crack model. *Finite Elements Anal Des*. 2013;73:77-95. https://doi.org/10.1016/j.finel.2013.05.005
20. Yoon JS, Zang A, Stephansson O, Hofmann H, Zimmermann G. Discrete element modelling of hydraulic fracture propagation and dynamic interaction with natural fractures in hard rock. *Procedia Eng*. 2017;191:1023-1031.
21. Hybrid FEM/DEM simulation of hydraulic fracturing in naturally-fractured reservoirs. In: ARMA: All Days of U.S. Rock Mechanics/Geomechanics Symposium. 2014. ARMA-2014-7107.
22. Zeng Q, Yao J, Shao J. An extended finite element solution for hydraulic fracturing with thermo-hydro-elastic-plastic coupling. *Comput Meth Appl Mech Eng*. 2020;364:112967.
23. Wong SW, Geilikman M, Xu G. The geomechanical interaction of multiple hydraulic fractures in horizontal wells. In: Bunger AP, McLennan J, Jeffrey R, eds. *Effective and Sustainable Hydraulic Fracturing*. IntechOpen; 2013.
24. Cordero JAR, Sánchez ECM, Roehl D, Pereira LC. Hydro-mechanical modeling of hydraulic fracture propagation and its interactions with frictional natural fractures. *Comput Geotech*. 2019;111:290-300.
25. Adachi J, Siebrits E, Peirce A, Desroches J. Computer simulation of hydraulic fractures. *Int J Rock Mech Min Sci*. 2007;44(5):739-757. https://doi.org/10.1016/j.ijrmms.2006.11.006
26. Lecampion B. An extended finite element method for hydraulic fracture problems. *Commun Numer Methods Eng*. 2009;25(2):121-133. https://doi.org/10.1002/cnm.1111
27. Shi F, Wang X, Liu C, Liu H, Wu H. An XFEM-based method with reduction technique for modeling hydraulic fracture propagation in formations containing frictional natural fractures. *Eng Fract Mech*. 2017;173:64-90. https://doi.org/10.1016/j.engfracmech.2017.01.025
28. Gordeliy E, Peirce A. Implicit level set schemes for modeling hydraulic fractures using the XFEM. *Comput Methods Appl Mech Eng*. 2013;266:125-143. https://doi.org/10.1016/j.cma.2013.07.016
29. Sheng M, Li G, Sutula D, Tian S, Bordas S. XFEM modeling of multistage hydraulic fracturing in anisotropic shale formations. *J Pet Sci Eng*. 2018;162:801-812. https://doi.org/10.1016/j.petrol.2017.11.007
30. Jafari A, Vahab M, Khalili N. Fully coupled XFEM formulation for hydraulic fracturing simulation based on a generalized fluid leak-off model. *Comput Methods Appl Mech Eng*. 2021;373:113447. https://doi.org/10.1016/j.cma.2020.113447
31. Zheng H, Pu C, Sun C. Study on the interaction between hydraulic fracture and natural fracture based on extended finite element method. *Eng Fract Mech*. 2020;230:106981. https://doi.org/10.1016/j.engfracmech.2020.106981
32. Cruz F, Roehl D, do Amaral Vargas E. An XFEM implementation in Abaqus to model intersections between fractures in porous rocks. *Comput Geotech*. 2019;112:135-146. https://doi.org/10.1016/j.compgeo.2019.04.014

33. Moës N, Belytschko T. Extended finite element method for cohesive crack growth. *Eng Fract Mech*. 2002;69(7):813-833. https://doi.org/10.1016/S0013-7944(01)00128-X
34. Currie I. *Fundamental Mechanics of Fluids*. 4th ed. Taylor & Francis; 2012.
35. Kirby B. *Micro- and Nanoscale Fluid Mechanics: Transport in Microfluidic Devices*. Cambridge University Press; 2010.
36. Yew C. *Mechanics of Hydraulic Fracturing*. Gulf Pub. Co.; 1997.
37. Batchelor GK. *An Introduction to Fluid Dynamics*. Cambridge University Press; 2000.
38. Spence DA, Sharp P. Self-similar solutions for elastohydrodynamic cavity flow. *Proc R Soc Lond A*. 1985;400:289-313. https://doi.org/10.1098/rspa.1985.0081
39. Duarte C, Oden J. An h-p adaptive method using clouds. *Comput Methods Appl Mech Eng*. 1996;139(1):237-262. https://doi.org/10.1016/S0045-7825(96)01085-7
40. Moës N, Dolbow J, Belytschko T. A finite element method for crack growth without remeshing. *Int J Numer Methods Eng*. 1999;46(1):131-150.
41. Dolbow J. *An Extended Finite Element Method with Discontinuous Enrichment for Applied Mechanics*. PhD thesis. Northwestern University; 1999.
42. Belytschko T, Chen H, Xu J, Zi G. Dynamic crack propagation based on loss of hyperbolicity and a new discontinuous enrichment. *Int J Numer Methods Eng*. 2003;58(12):1873-1905.
43. Cahill L, Natarajan S, Bordas S, O'Higgins R, McCarthy C. An experimental/numerical investigation into the main driving force for crack propagation in uni-directional fibre-reinforced composite laminae. *Compos Struct*. 2014;107:119-130. https://doi.org/10.1016/j.compstruct.2013.05.039
44. Erdogan F, Sih G. On the crack extension in plates under plane loading and transverse shear. *J Fluids Eng*. 1963;85(4):519-525.
45. Tanaka K. Fatigue crack propagation from a crack inclined to the cyclic tensile axis. *Eng Fract Mech*. 1974;6(3):493-507. https://doi.org/10.1016/0013-7944(74)90007-1
46. Papanastasiou P. An efficient algorithm for propagating fluid-driven fractures. *Comput Mech*. 1999;24:258-267. https://doi.org/10.1007/s004660050514
47. Chen L, Kuang J. A modified linear extrapolation formula for determination of stress intensity factors. *Int J Fract*. 1992;54(1):R3-R8.
48. Nagashima T, Omoto Y, Tani S. Stress intensity factor analysis of interface cracks using X-FEM. *Int J Numer Methods Eng*. 2003;56(8):1151-1173.
49. Natarajan S, Bordas S, Mahapatra D. Numerical integration over arbitrary polygonal domains based on Schwarz-Christoffel conformal mapping. *Int J Numer Methods Eng*. 2009;80(1):103-134.
50. Parks D. A stiffness derivative finite element technique for determination of crack tip stress intensity factors. *Int J Fract*. 1974;10(4):487-502.
51. Rybicki E, Kanninen M. A finite element calculation of stress intensity factors by a modified crack closure integral. *Eng Fract Mech*. 1977;9(4):931-938.
52. Shih C, Asaro R. Elastic-plastic analysis of cracks on bimaterial interfaces: part I-small scale yielding. *J Appl Mech*. 1988;55(2):299-316.
53. Yau J, Wang S, Corten H. A mixed-mode crack analysis of isotropic solids using conservation laws of elasticity. *J Appl Mech*. 1980;47(2):335-341.

How to cite this article: Wang Y, Javadi AA, Fidelibus C. A hydro-mechanically-coupled XFEM model for the injection-induced evolution of multiple fractures. *Int J Numer Anal Methods*. 2023;1-20. https://doi.org/10.1002/nag.3527